crystals

MDPI

Article

Analysis of Radiation Hardening Effect of Ferritic Martensitic Steel Based on Bayesian Optimization

Yue He, Jiaming Bao, Shi Wu, Bing Bai *, Xinfu He and Wen Yang

Reactor Engineering Technology Research Institute, China Institute of Atomic Energy, Beijing 102413, China; 17749736232@163.com (Y.H.); 13278883326@163.com (J.B.); wusmmm@163.com (S.W.); hexinfu@cnncmail.cn (X.H.); ywhyangwen@163.com (W.Y.)

* Correspondence: bbai@cnncmail.cn; Tel.: +86-186-0075-5420

Abstract

Ferritic/martensitic (F/M) steel is a candidate material for key structures in fourth-generation nuclear energy systems (such as fusion reactors and fast reactors). Irradiation hardening behavior is a core index to evaluate the material's stable performance in a high-neutron-irradiation environment. In this study, based on 2048 composition and property data, a correlation model between key elements and their interactions and irradiation hardening in F/M steel was constructed using a Bayesian optimization neural network, which realized quantitative prediction of the effect of composition on hardening behavior. Studies have shown that the addition of about 9.0% Cr, about 0.8% Si, Mo content higher than about 0.25%, and the addition of Ti, Mn can effectively suppress the irradiation hardening of F/M steel, while the addition of N, Ta, and C will aggravate its irradiation hardening, and the addition of W and V has little effect on the irradiation hardening of F/M steel. There is an interaction between the two elements. C-Cr has a strong synergistic mechanism, which will cause serious hardening when the content is higher than 0.05% and the Cr content is higher than 10%. Cr-Si has a strong antagonistic mechanism, which can achieve the comprehensive irradiation hardening effect in the 9Cr-0.8Si combination. N-Mn needs N controlled lower than 0.01%. Mo-W needs to control Mo content higher than 0.5% to alleviate irradiation hardening. There is a weak synergistic effect in Si-V; when the content is between 0.3% and 0.8% and the V content is between 0.2% and 0.3%, it can assist in optimizing the composition of F/M steel. Through the optimization of multi-element combination, the composition of F/M steel with lower irradiation hardening can be designed.

Keywords: ferritic martensitic steel; Bayesian optimization; irradiation hardening; performance prediction

check for updates

Academic Editor: José L. García

Received: 21 August 2025
Revised: 28 September 2025
Accepted: 29 September 2025
Published: 30 September 2025

Citation: He, Y.; Bao, J.; Wu, S.; Bai, B.; He, X.; Yang, W. Analysis of Radiation Hardening Effect of Ferritic Martensitic Steel Based on Bayesian Optimization. *Crystals* **2025**, *15*, 864. https://doi.org/10.3390/cryst15100864

Copyright: © 2025 by the authors. Licensee MDPI, Basel, Switzerland. This article is an open access article distributed under the terms and conditions of the Creative Commons Attribution (CC BY) license (https://creativecommons.org/licenses/by/4.0/).

1. Introduction

In recent years, nuclear energy technology has made great progress, and the unit capacity and thermal efficiency of fourth-generation reactors, including fusion and fast reactors, have been continuously improved, posing higher requirements for the performance of structural materials in extreme service environments. The first wall and cladding structure materials of reactors and the fuel cladding and component materials of fast reactors all face multiple harsh conditions such as high-flux neutron irradiation, high temperature, and thermo-mechanical fatigue corrosion. In particular, in fusion reactors, high-flux 14 MeV neutron irradiation and transmutation-produced helium, hydrogen, and other impurity

elements will cause significant radiation, resulting in radiation defects, helium blisters, and other defects in the materials, which will significantly reduce or even degrade the mechanical properties such as strength and toughness of the materials, thereby reducing the life of the materials in the fusion reactor and affecting its normal operation and safety. Similarly, in fast neutron reactors, high-energy neutron irradiation also induces significant radiation effects, requiring materials to have excellent radiation resistance and microstructure stability. Currently, the candidate materials recommended for fuel cladding and core structure of fourth-generation reactors [1,2] internationally are F/M steel, ODS steel, austenitic stainless steel, nickel-based alloys, refractory alloys ceramic materials, and graphite materials. Compared with other candidate materials, F/M steel has the advantage of a better comprehensive performance in the working environment of advanced reactors. Compared with aenitic stainless steel and nickel-based alloys, the larger thermal conductivity of 9–12% Cr ferritic/martensitic steel is conducive to improving the thermal efficiency of the reactor, its better dimensional stability, high-temperature strength, and creep rupture strength can improve the safety of the reactor during long-term operation, and its better high-temperature corrosion resistance can better adapt to the chemical environment in the core. In addition, ferritic/martensitic steel has high economic benefits, and its manufacturing cost is far lower than that of nickel-based alloys, refractory alloys, and ODS steel. Therefore, 9–12% Cr ferritic/martens steel is considered to be the first choice of candidate material for fuel cladding and core structure materials of fourth-generation reactors [3]. Among them, low-activation ferritic/martensitic steel (RAFM) has the advantages of a low irradiation swelling coefficient, good thermal conductivity, excellent irradiation swelling resistance, and relatively mature process foundation, and is widely considered to be a candidate material for key components of fusion and fast reactors.

The influence degree of irradiation on the comprehensive performance of F/M steel is an important basis for evaluating the applicability of F/M steel in advanced reactors, and reducing the effect of irradiation hardening is of great research significance for improving the comprehensive service performance of F/M steel under extreme conditions such as nuclear reactors. Radiation hardening refers to the significant increase in the yield strength and tensile strength of a material when subjected to fast neutron irradiation, and the yield strength can even approach the fracture strength, resulting in plastic loss of the material [4]. The essential reason for this is closely related to the various defects introduced into the crystal by irradiation, such as defect size and density. Chaouadi [5] studied the tensile strength of Eurofer97 low-activation material at 300 °C and an irradiation dose of 0.3–2.1 dpa. The results showed that with the increase in neutron irradiation, the yield strength of the material increased and the ductility significantly decreased, indicating that irradiation would exacerbate the deterioration of the mechanical properties of F/M steel. In addition, different irradiation temperatures will also result in different irradiation effects on F/M steel. Under low-temperature irradiation (approximately 300 °C), point defects generated by irradiation in F/M steel hinder the movement of dislocations, causing the material to harden or become brittle [6]; however, high-temperature irradiation (about 500 °C) can induce segregation of alloy elements in F/M steel, and the rapid migration of atoms at dislocation, grain boundary, and other defects is prone to generate cavities, which will lead to radiation swelling [7]. These irradiation effects can directly affect the mechanical properties and corrosion resistance of F/M steel. The study by Gaganidze et al. showed that the irradiation hardening of F82H and EUROFER97 steels after neutron irradiation at 330 °C reached saturation at irradiation doses of 30–40 dpa [8,9]. Due to the large number of dislocation loops generated by irradiation, the hardening strength and DBTT variables of the irradiated samples decreased after high-temperature tempering, indicating that post irradiation tempering restored the irradiation defects. Q. Huang et al. [10] used an optical

microscope and transmission electron microscope (TEM) to observe the microstructure of CLAM steel after heat treatment. The optical microscope images showed that no delta ferrite appeared in CLAM, while the TEM images showed that the microstructure of CLAM was composed of fine columnar martensite phase and well-annealed martensite phase, and the columnar structure was very fine. The results of a performance test showed that CLAM showed an excellent performance before irradiation. Qunying Huang et al. [11] considered that the MX precipitation phase of F/M steel was stable in long-term operation at a high temperature, and a small amount of titanium was added to CLAM steel. It was found that the addition of titanium element could simultaneously improve the strength and ductility of material. The improvement of strength at room temperature was the result of grain refinement and the increase in MX carbide caused by Ti addition, while an improvement in ductility was caused by refinement and the decrease in $M_{23}C_6$ carbide. In addition, the small addition of Zr, Ce, and Ta could also significantly improve the microstructure stability of material under high-temperature conditions. From the above, it can be found that the irradiation dose, irradiation temperature, microstructure, and alloy composition can all affect the irradiation hardening effect of RAFM steel by different mechanisms.

The implementation of the Materials Genome Project provides a new paradigm for solving the problem of radiation damage. Machine learning can make full use of existing experimental data to achieve accurate prediction of material service performance without clear mechanism principles, reducing the time and cost required for experiments. The three-dimensional convolutional neural network developed by Castin et al. [12] successfully predicted the nonlinear relationship between RAFM steel irradiation hardening and dislocation density evolution; Cottrell et al. [13] used artificial neural networks to predict the temperature changes in ductile brittle transition caused by irradiation in low-activation steel; and Bai Bing et al. [14] used deep neural networks to predict the radiation hardening performance of oxide dispersion strengthened (ODS) alloy, a candidate material for the first wall structure of fusion reactors. The ODS steel irradiation swelling prediction model constructed through transfer learning shortened the experimental verification period by 60%. Moreover, systematic assessment of the influence of irradiation on the tough-brittle transition behavior of RAFM steels was conducted by Wangengxin et al. [15,16]. Their developed integrated-learning model revealed the positive role of Ta and W elements and the complicated influence regularity of Cr on the inhibition of irradiation embrittlement by predicting DBTT. In terms of irradiation hardening, this team's research showed that the hardening peaked at about 315 °C and then decreased at higher temperatures due to microstructure recovery, and the potential of Ta in mitigating irradiation hardening was confirmed through-scale data mining, which provides a valuable database and model basis for understanding the performance evolution of RAFM steels under irradiation conditions. The above progress shows that the data-driven method can effectively decouple the coupling effect of multiple factors, and open up new avenues for the design of radiation-resistant materials for fusion environments.

Compared with the above experimental research and traditional empirical models, the Bayesian optimization BP neural network method adopted in this study shows unique advantages in predicting the radiation hardening of F/M steel, and its core innovation lies in the automatic search for the optimal hyperparameters of the neural network through Bayesian optimization, avoiding blindness manual tuning, and thus obtaining a more robust and generalized prediction model on limited experimental data. The dataset we constructed covers a broader range of material compositions, including key RAFM steels such as Eurofer97, F82H, and CLAM, and some traditional F/M steels, which enhances the generalization ability of the model in a wide range of composition spaces and irradiation conditions. The prediction accuracy of the model in this study (measured by R^2 and

RMSE) is significantly improved compared to traditional regression models, not only achieving accurate prediction of radiation hardening of F/M steel, but also quantifying the contribution of characteristic elements to radiation hardening through feature importance analysis, single-element prediction, and recognition of binary element interaction effects, revealing the key component intervals and their synergistic/antagonistic mechanisms. This study aims to establish a set of component methods applicable to a variety of F/M steel systems, providing theoretical support and data references for the performance optimization and new material development of structural materials for advanced nuclear energy systems such as reactors and fast reactors.

2. Data Collection and Descriptive Analysis

The data of this article comes from experiments and literature data collection. The irradiated hardening data collected from ferritic/ensitic steels include 2048 samples and 34 types of composition characteristics (including main elements such as Cr, W, Mo, etc., and trace elements such as C, Si, P, etc.), and the target variable is the yield strength. Since the ideal material for the first wall and cladding structure of the fusion reactor is low-activation ferritic/martensitic steel, the data contains F82H, EUROFER-97, fourth-generation low-activation ferritic/ensitic steel, and domestic CLAM steel, and there are composition characteristic data such as low-activation elements W, V, Ta, Cr, Ti, C, etc. Some obvious characteristic variables may have some missing values and abnormal values in the process of data collection (such as C, Cr elements missing or content anomalies). This kind of data is for modeling, which will lead to a poor prediction effect and low prediction accuracy of the model, and it is impossible to obtain a prediction model that can help future research and actual production. In order to accurately obtain the correlation between the alloy composition and its neutron irradiation hardening, by deleting the component missing values and abnormal values, finally, 2014 data were obtained. Among the 2014 samples, the proportion of zero data values of As, Bi, Ce, Co, Ce, and other element characteristics is $\geq$90%, because the existing $\leq$ 10% data volume cannot cover most of the samples and adding these feature data in the model training will make the model over-characterized, reducing the generalization and prediction of the model itself, so these redundant feature data are removed, and finally 16 composition characteristics are obtained and four key variables Irr_T(K), Irr_Dpa, Test_T (K), and YS (MPa) are added. The interval distribution of each characteristic is shown in Table 1. Through the analysis of the key component characteristics of F/M steel, the dataset is manually classified according to the component characteristics and then summarized in Table 2. The source distribution of the dataset is shown in Figure 1.

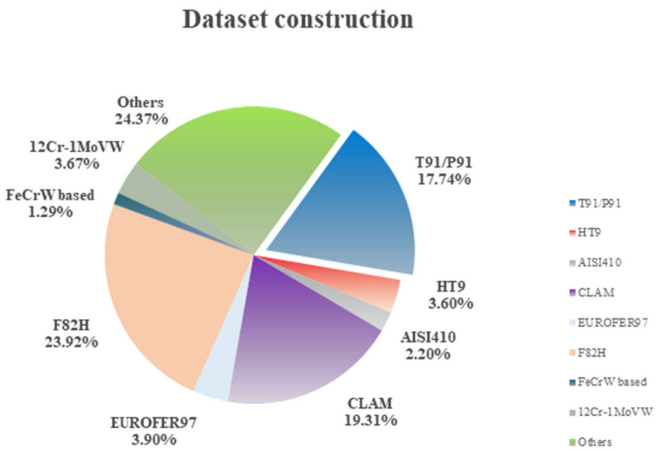


Figure 1. Dataset composition pie chart.

Table 1. The distribution of each characteristic interval obtained by screening.

Feature Variable	Component Interval		
	Minimum	**Maximum**	**Average Value**
C (wt%)	0	0.2	0.0962
Cr (wt%)	4.9	18	8.40801
W (wt%)	0	3	1.42886
Mo (wt%)	0	1	0.14519
Ta (wt%)	0	0.54	0.06367
V (wt%)	0	0.314	0.18045
Si (wt%)	0	0.37	0.05689
Mn (wt%)	0	1.13	0.16789
N (wt%)	0	0.06	0.00409
Al (wt%)	0	0.054	0.00196
B (wt%)	0	8.5	0.57755
Nb (wt%)	0	1.6	0.01577
Ni (wt%)	0	2	0.05792
P (wt%)	0	7	1.12836
S (wt%)	0	5	1.03355
Ti (wt%)	0	2.5	0.08646
Irr_T (K)	237	925	402.27146
Irr (dpa)	0	90	3.72716
Test_T (K)	123	1033	533.88209
YS (MPa)	117	4100	526.46504

Table 2. Data sources.

Classification	Steel Grade	Component Characteristics	Quantity	Percentage
Traditional F/M steel	T91/P91	Cr content 8.5~9.5%; High Mo content 0.85~1.05%	356	17.77%
	HT9	High Cr content 11–13%; High Mo content 0.8–1.2%	73	3.60%
	AISI410	High Cr content 11.5~13.5%; Mo content $\leq$ 0.5%	44	2.2%
Low activation F/M steel	CLAM steel	W content 1.0~1.5%; Ta content 0.12~0.18%	389	19.31%
	EUROFER97	W content 0.9~1.1%; Ta content 0.08~0.12%	78	3.90%
	F82H	W content 1.8~2.2%; Ta content 0.03~0.05%	482	23.92%
	FeCrW based	W content 1.8~2.2%; Ta content 0.03~0.05%; Si content 0.3~0.7	26	1.29%
	12Cr-1MoVW	W content 1.0~2.0%; Ta free	74	3.67%
Other traditional steel	Others	Cr content span is large 0.1~25%; Mo/W can reach >5%.	493	24.47%

3. Data Correlation Analysis

From the research and the obtained dataset, it can be seen that the various alloy compositions of F/M steel do not individually affect its mechanical properties. Some elements may also couple and affect its mechanical properties in a certain mass fraction ratio. Therefore, this article needs to conduct correlation analysis on the obtained dataset. Correlation analysis can assist in testing the relationship between component characteristics and target variables, and can also help identify which variables may have a significant impact on prediction results, thereby guiding feature selection and model construction. If the correlation between the two is low, it can be removed during the establishment of the regression model. Secondly, correlation analysis can also assist in analyzing the collinearity between features. If there is a strong correlation between two features, coupling effects can be considered.

There are three commonly used methods for calculating the correlation coefficient of feature data in machine learning, namely Pearson linear correlation coefficient, Spearman rank correlation coefficient, and Kendall rank correlation coefficient [17]. The Kendall rank correlation coefficient is used for correlation analysis of categorical variables, and, therefore, is not considered in this article. The Pearson linear correlation coefficient is applicable to data that simultaneously satisfies continuous data, a normal distribution, and a linear relationship. The Spearman rank correlation coefficient does not have strict requirements for data distribution and belongs to non-parametric statistical methods. Its applicability is wider than the Pearson linear correlation coefficient, and it uses the rank size of variables for correlation analysis. Due to the fact that the Spearman rank correlation coefficient is based on data sorting rather than actual values, it is more robust to nonlinear relationships and can capture more complex correlations between data [18]. Therefore, this paper uses the Spearman rank correlation coefficient for correlation analysis.

The calculation formula of this method is shown in Equation (1), where x and y represent two features, respectively, and the calculation results are between −1 and 1. The larger the absolute value of the correlation coefficient, the stronger the correlation between the two variables, and vice versa, the weaker the correlation. Positive values show a positive correlation, and negative values show a negative correlation.

$$\rho_{xy} = \frac{\sum_{i=1}^{n}(x_i - \overline{x})(y_i - \overline{y})}{\sqrt{\sum_{i=1}^{n}(x_i - \overline{x})^2 \sum_{i=1}^{n}(y_i - \overline{y})^2}} \quad (1)$$

In the formula, i is the sample number; n is the total number of samples; ρ_{xy} is the calculated correlation coefficient; $\overline{x}$ is the mean of feature x; and $\overline{y}$ is the mean of feature y.

As shown in Figure 2, the thermodynamic diagram was formulated using the Spearman rank correlation and Pearson linear correlation for the dataset used in this experiment. The color intensity represents the magnitude of the correlation, blue represents positive correlation, and red represents negative correlation.

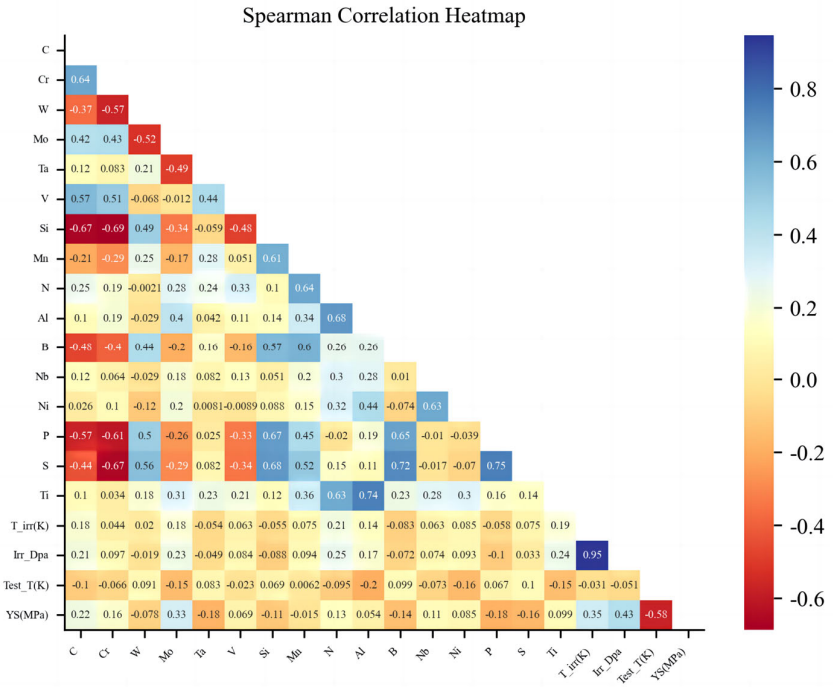


Figure 2. Correlation analysis heat map.

According to the research, the role of C in RAFM steel is divided into two aspects. Firstly, it dissolves in the high-temperature aenite, which has a significant inhibitory effect on the formation of ferrite, and obtains martensite with carbon supersaturation, which provides a guarantee for phase change [19]; on the other hand, C, as a key interstitial atom, can interact with alloy elements such as Cr, Fe, V, Ta, etc., to form dispersedly distributed $M_{23}C_6$ and MX carbides [20], so the material has a good high-temperature strength and obtains a higher yield strength after radiation. In addition, the research team of S. Jitsukawa [21] showed that the two main factors affecting the irradiation hardening of F82H are the test temperature and the irradiation dose, and the yield strength gradually increases with an increase in the irradiation dose, showing a positive correlation. The Spearman rank correlation calculation shows that the correlation coefficient of C is 0.22, indicating a positive correlation between the C element and yield strength. The correlation coefficients of irradiation dose and test temperature are 0.43 and −0.58, respectively, with absolute values higher than those of other characteristic components, indicating that they have the greatest impact on yield strength, which is consistent with the research results.

Considering that certain elements can also couple and affect their mechanical properties with a certain mass fraction ratio, by analyzing the changes in yield strength jointly affected by the combination of two elements, it can be concluded that under specific temperature conditions, the composition design of F/M yield strength reaches a certain range. Based on the correlation thermal analysis chart, this article selected ten sets of two elements with strong positive and negative correlations.

As shown in Figure 2, there is a positive correlation between P and S, Al and Ti, S and B, S and Si, Al and N, P and Si, P and B, C and Cr, N and Mn, and Ti and N, and the correlation coefficients are shown in Table 3.

Table 3. Positive correlation of dual element components.

Element 1	Element 2	Spearman Rank Correlation Coefficient
P	S	0.75
Al	Ti	0.74
S	B	0.72
S	Si	0.68
Al	N	0.68
P	Si	0.67
P	B	0.65
C	Cr	0.64
N	Mn	0.64
Ti	N	0.63

Research has shown that in F/M steel, P, S, and Si elements undergo segregation at grain boundaries, leading to embrittlement. P and S have a large negative charge and a strong attraction to electrons, causing an increase in charge density and electron localization, which is not conducive to grain boundary bonding. P and S, S and Si, and P and Si have a synergistic strengthening effect on weakening grain boundary bonding, showing a positive correlation. Some studies [22,23] suggest that a structure similar to Fe_3P compound is formed around the P atoms that segregate at the α-Fe grain boundary, while S mainly forms a structure similar to FeS compound [24]. Grain boundary segregation will weaken the grain boundary binding force, leading to brittleness; Huang Mengzhe et al. [25] studied the effects of different concentrations of Si, P, and S on grain boundaries, and found that due to the differences in the atomic size and electron gain/loss ability of different elements, their effects on grain boundaries also vary greatly. Low-concentration Si has an enhancing effect on the bonding of grain boundaries, resulting in an increased strength

and toughness; however, P and S are not conducive to the bonding of grain boundaries. As the concentration increases, high concentrations of Si, P, and S all weaken the binding of grain boundaries, with Si and S showing a more pronounced weakening effect with an increasing concentration; the weakening effect of P shows a trend of first decreasing and then increasing with an increasing concentration, mainly due to the bonding of P at a certain concentration causing grain boundary misalignment and reducing the weakening effect. The segregation energy of B is relatively small, making it easy for segregation to occur at grain boundaries. B atoms can change the electronic structure of grain boundaries, reduce grain boundary energy, and weaken grain boundary bonding. Therefore, P and S have a strengthening effect on the weakening of grain boundary bonding by element B, and also show a positive correlation.

The C atom plays a role in precipitation strengthening in F/M steel, and the generation of precipitates has a pinning effect on dislocations; Cr atoms can increase the cohesion of grain boundaries and enhance their bonding, both of which have a strengthening effect on grain boundary bonding, showing a positive correlation.

According to Figure 2, Cr and Si, Cr and S, C and Si, Cr and P, Cr and W, C and P, Mo and W, Ta and Mo, C and B, and Si and V are all negatively correlated, and the correlation coefficients are shown in Table 4.

Table 4. Negative correlation of dual element components.

Element 1	Element 2	Spearman Rank Correlation Coefficient
Cr	Si	−0.69
Cr	S	−0.67
C	Si	−0.67
Cr	P	−0.61
Cr	W	−0.57
C	P	−0.57
Mo	W	−0.52
Ta	Mo	−0.49
C	B	−0.48
Si	V	−0.48

Lv Zhiqing [26] found, through the study of solute elements on the continuous behavior of grain boundaries, that Cr atoms can increase the cohesion of grain boundaries, and the addition of Cr elements significantly reduces the low-charge-density region of grain boundaries. The segregation of P, S, and Si elements at grain boundaries results in a significant negative charge, leading to an increase in charge density at the grain boundaries and a clear negative correlation with Cr elements. Among the three elements, Si has the smallest electron attraction, therefore, the negative correlation between Si and Cr is the strongest. Through the positive correlation analysis in the previous text, it can be seen that both C and Cr elements strengthen the bonding at grain boundaries, while P, Si, and B elements segregate and weaken the bonding force at grain boundaries. Therefore, Si and P are negatively correlated with C, and similarly, Si has a smaller electron attraction, resulting in a stronger negative correlation with C. In addition, adding microalloying elements such as Ti, V, and Mo to F/M steel can form small precipitates and refine grains in the steel, which can improve strength.

By analyzing the correlation coefficients of the two elements, the accuracy of the Spearman rank correlation coefficient analysis dataset was further verified, providing a basis for designing radiation-resistant F/M steels with certain composition ratios under specific conditions in the future.

Therefore, according to Figure 2, it can be found that from the data alone, components such as W, Ta, Si, Mn, B, P, and S are not favorable to the yield strength, and an increase in content may degrade the yield strength of F/M steel; components such as C, Cr, Mo, V, N, Al, Nb, Ni, and Ti show a positive correlation, which is beneficial to the improvement of F/M yield strength. Combining the adequacy of the data samples and the magnitude of the correlation coefficient, as well as the analysis of the positive and negative correlation coefficients of the binary elements and the analysis of the common effect of each element on the yield strength, this paper selects the C element (Spearman rank correlation coefficient is 0.22), N element (Spearman rank correlation coefficient is 0.13), and Si element (Spearman rank correlation coefficient is −0.11) in trace elements (mass fraction $\leq 0.1\%$) for prediction analysis. In alloying elements, the Cr element (Spearman rank correlation coefficient is 0.16), W element (Spearman rank correlation coefficient is −0.078), Mo element (Spearman rank correlation coefficient is 0.33), V element (Spearman rank correlation coefficient is 0.069), Ti element (Spearman rank correlation coefficient is 0.099), Ta element (Spearman rank correlation coefficient is −0.18), and Mn element (Spearman rank correlation coefficient is −0.015) are selected for prediction analysis. On the basis of the prediction results of single elements, combined with the conclusion of binary elements correlation, Section 6 will predict the influence of binary elements interaction on the radiation hardening effect.

Based on the current irradiation temperature in the reactor reaching above 550 °C/823 K, this article selects 550 °C/823 K for the irradiation temperature and 25 °C/298 K for the experimental temperature. According to the actual design requirements, an irradiation dose of 20 dpa is selected. Combining the correlation coefficient and considering low-activation elements, the influence of single components Mo, C, Ta, Cr, N, Si, Ti, V, Mn, and W with an irradiation dose of 20 dpa on the irradiation hardening trend of ironclad steel after irradiation is studied.

4. Bayesian Optimization for BP Neural Network Training Optimization

Artificial neural networks (ANNs) are a computational model inspired by the biological nervous system to simulate the interactions between neurons in the human brain [27]. Among them, the backpropagation neural network (BP) is one of the common artificial neural network models, which is a multi-layer feedforward neural network trained based on an error backpropagation algorithm [28]. The BP neural network consists of an input layer, a hidden layer, and an output layer, where the hidden layer can have multiple layers. The BP neural network passes the input signal to the output layer through forward propagation, then calculates the output error through the backpropagation algorithm, and uses gradient descent to adjust the connection weights in the network to minimize the error function. The structure of the BP neural network is shown in Figure 3.

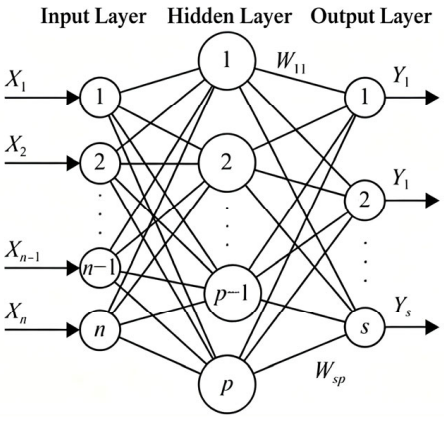


Figure 3. BP neural network structure.

Bayesian optimization, as an effective method for hyperparameter optimization, can guide the next parameter selection by establishing a posterior probability of the objective function under uncertainty, thus finding the global optimal solution with fewer evaluations. This paper uses Bayesian optimization to automatically tune the key structural parameters of the BP neural network, aiming to improve the model's prediction performance and generalization ability. The number of neurons in the hidden layer (units) of the BP neural network directly affects the model's representation and capabilities. Too few neurons may lead to model underfitting, failing to capture the complex features in the data, while too many neurons will significantly increase the risk of overfitting. Meanwhile, the number of training epochs (epochs) is crucial for the model's generalization ability and training efficiency. Too few epochs will result in an insufficiently trained model (underfitting), while too many will lead to the model overfitting the training data (overfitting). This paper constructs a Bayesian optimization process with the goal of "minimizing the mean squared (MSE) of the validation set", sets the search boundary of the number of neurons (units) from 50 to 300, and sets the search boundary of the number of training epochs (epochs) from 50 to 200. In the optimization, 10 groups of initial parameter combinations are randomly sampled and evaluated, and then 10 iterations of optimization are performed on this basis. By balancing "exploration" and "exploitation" through the Gaussian process surrogate model, the optimal combination is finally determined. This process ensures that the determined hyperparameters are the optimal solution within the given search space based on the validation set performance, effectively avoiding the subjectivity and blindness manual tuning and enhancing the objectivity and reproducibility of the model building process. In addition, to improve the comparability of features and the accuracy of the model and to speed up the calculation, the input data is often normalized. The purpose of normalization processing is to limit input parameters of different orders of magnitude to within the same range, thereby reducing the impact differences caused by orders of magnitude. The specific conversion formula for adjusting all feature data in this article to the interval of [0, 1] is as follows:

$$X = \frac{x - x_{\min}}{x_{\max} - x_{\min}}(U - L) + L \tag{2}$$

In the formula, X is the normalized data; X is the raw data; U is the upper limit of the interval; and L is the lower limit of the interval.

To evaluate the machine learning model, the loss function, training set, and test set are generally used to visualize the evaluation, as shown in Figure 4, where Figure 4a is the training set variance and test set variance after Bayesian optimization of the BP neural network model. It is found that the error of the model basically converges and stabilizes after approximately 40 epochs of the entire network. Figure 4b,c are the scatter plots of the predicted value and the true value in the set and test set, where the RMSE of the training set is 0.0145, MAE is 0.0876, and R^2 Score is 0.8723, and the RMSE of the test set is 0.0218, MAE is 0.1023, and R Score is 0.8124. It can be seen that the experimental value and the predicted value are in good agreement and the model performance is high. Finally, the coefficient of determination R^2 is used for evaluation, and the calculation of R^2 is as shown in Equation (3), as follows:

$$R^2 = 1 - \frac{\sum_{i=1}^{n}(y_i - \hat{y}_i)^2}{\sum_{i=1}^{n}(y_i - \overline{y})^2} \tag{3}$$

In the formula, y_i is the true value of the i-th sample; $\hat{y}$ is the regression value of the i-th sample; and $\overline{y}$ is the mean of sample y.

The R^2 value calculated in this article ranges from 0 to 1, and the final R^2 value reaches 0.8124.

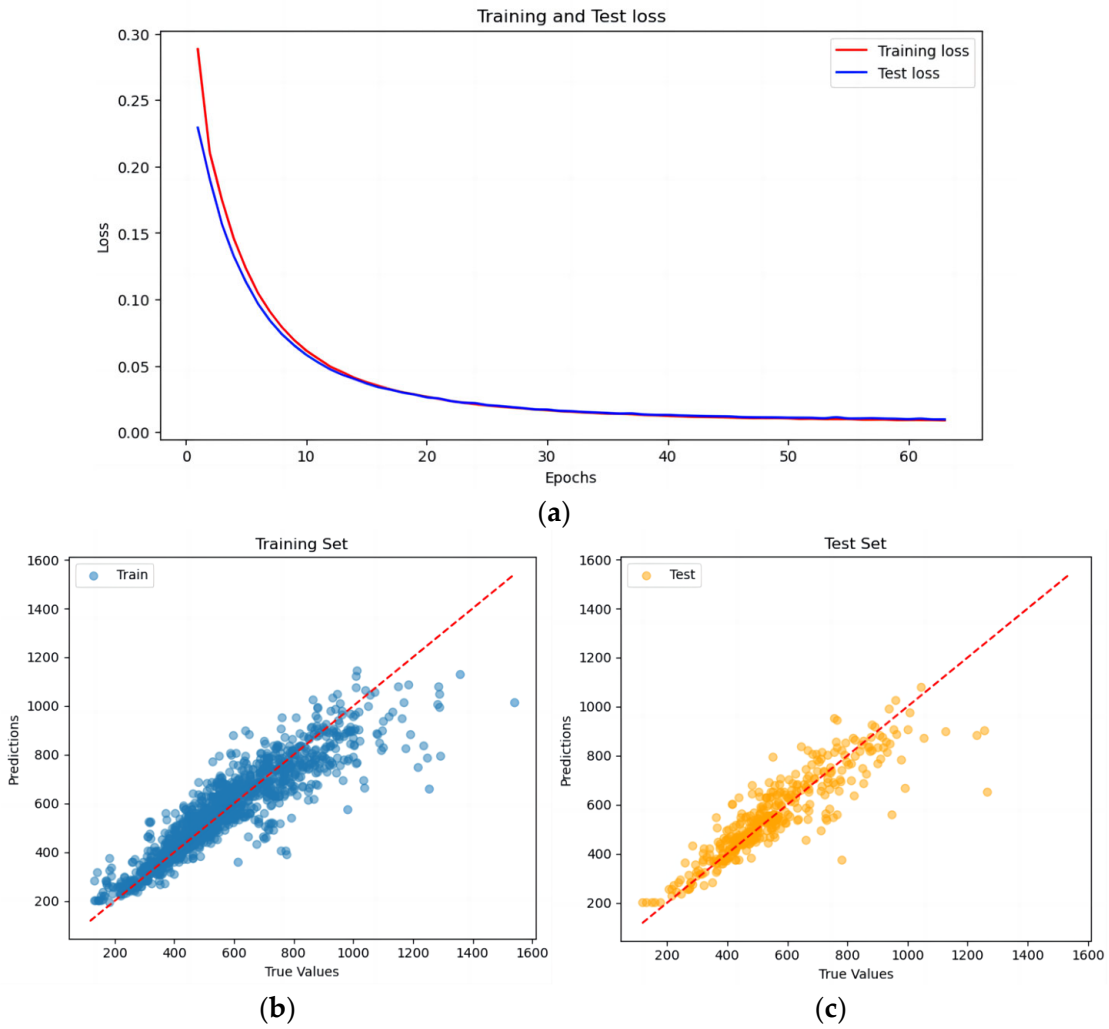


Figure 4. Model evaluation. (**a**) Loss function curves for training and testing sets; (**b**) scatter plot of predicted value and true value in the training set; and (**c**) scatter plot of predicted value and true value in the training set.

5. SHAP Analysis

SHAP is an explanation method for machine learning models proposed by Lundberg et al. [29], which generates a value (also SHAP value) for each input feature, accurately quantifying the contribution of the feature to the final output of the model. Positive values indicate that it is beneficial to the generation of a prediction value, negative values indicate that it is not conducive to the generation of the prediction value, and the absolute value represents the weight of influence. In order to evaluate the feature importance, as shown in Figure 5, the SHAP value is calculated for all features and the average of the absolute values is taken, which gives the distribution of the features. It is found that the test temperature has the greatest effect on the target variable, followed by the irradiation temperature dose. Among the component features, the Mo element has the most significant effect, followed by V, N, Si, and other elements, while the Cr, Ta, P, S, and C elements have a relatively small impact. This is corroborated by the conclusion of the correlation analysis, increasing the accessibility of the model.

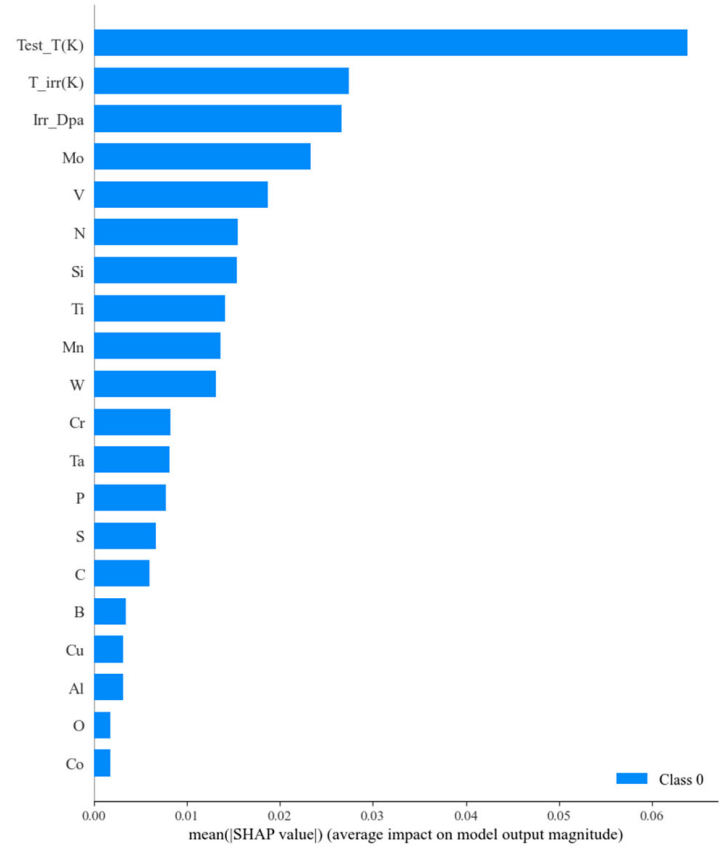


Figure 5. SHAP average for all features.

To further reveal the mechanism of the interaction between key features and prediction results, the SHAP scatter plot of the test temperature was drawn. Figure 6a shows that the SHAP value of Test_T and the feature value present a significant negative correlation trend, which indicates that the higher the test temperature, the more the predicted yield strength value is affected in the model prediction. According to the research findings of Huang [30], CLAM steel has a lower ductile–brittle transition (DBTT) after irradiation at 480 °C and hardening is more obvious, indicating that the recovery temperature window is around 480 °C at higher temperatures, the activity of point defects is enhanced, and some defects disappear, which affects the degree of hardening and the recovery of DBTT. This phenomenon reveals that a higher test temperature promotes the annealing and disappearance of irradiation defects, defects are the main source of hardening, and when defects are reduced, the yield strength decreases accordingly. Addition, Figure 6b shows the relationship between the SHAP value of the Mo element and its content, and it can be seen that there is a significant nonlinear relationship between Mo and yield strength. When the Mo content tends to 0, it has little effect on the yield strength; while in the high Mo area, it has a significant positive effect on yield strength. This phenomenon is related to the composition of the dataset used in this article. In the low Mo area, the data points mainly correspond to RAFM steel. RAFM steel strictly limits or removes the Mo element to reduce long-term radioactivity and replaces it with low-activation elements such as W, V, etc. [31]. The data points in the high Mo area mainly correspond to traditional F/M steel. In traditional F/M steel, the Mo element is a key solid-solution-strengthening and carbide-forming element [32].

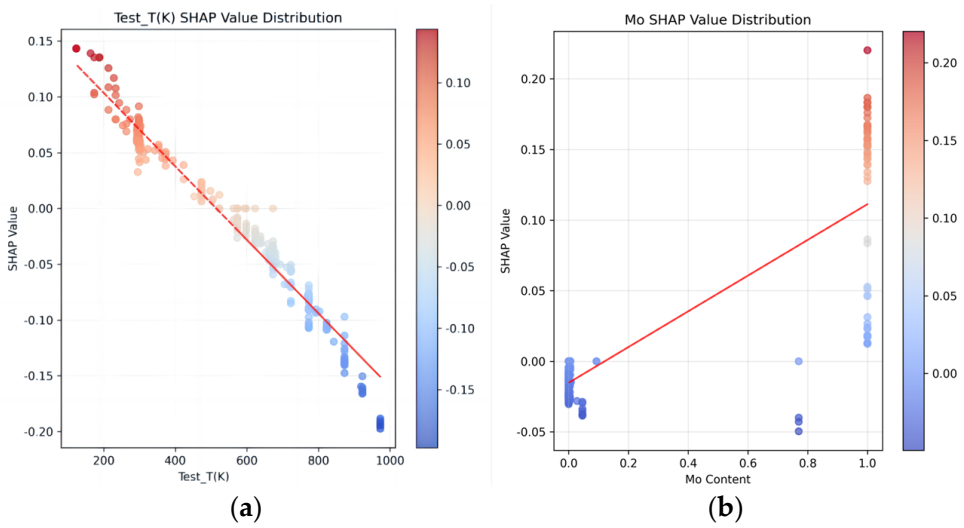


Figure 6. SHAP dependency graph. (**a**) SHAP dependency graph of Test_T and (**b**) SHAP-dependent graph of Mo element.

Based on the above analysis, SHAP not only provides the ranking of feature importance, but also reveals the complex influence mechanism of key process parameters and alloy elements on the yield strength of F/M steel, further enhancing the depth and reliability of the model interpretation.

6. Predicting the Correlation Between Specific Components and Radiation Hardening

According to experimental experience, the main factors affecting irradiation hardening are irradiation dose, irradiation temperature, and test temperature. Therefore, we first use the constructed model to establish the correlation between irradiation dose and irradiation temperature, as well as the relationship between test temperature and the yield strength of F/M steel for prediction, as shown in Figures 7–9.

As shown in Figure 7, with an increase in irradiation dose, the yield strength shows an upward trend and stabilizes after a 60 dpa irradiation dose, indicating that the degree of irradiation hardening has intensified. Chaouadi [5] studied the tensile strength of Eurofer97 low-activation material at 300 °C and an irradiation dose of 0.3–2.1 dpa. The results showed that with an increase in neutron flux, the yield strength of the material increased and the ductility significantly decreased, consistent with the predicted results of the model.

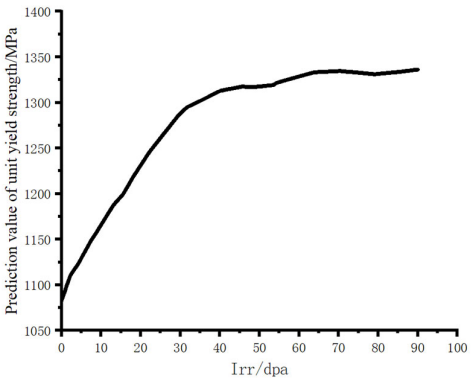


Figure 7. Effect of irradiation dose on yield strength.

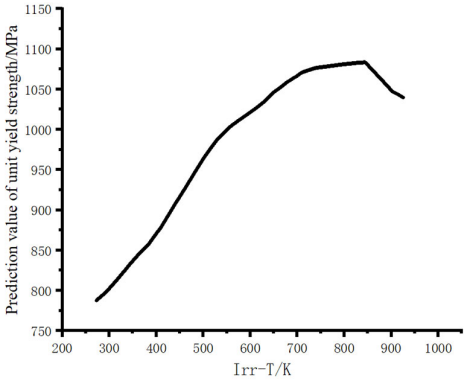


Figure 8. Effect of irradiation temperature on yield strength.

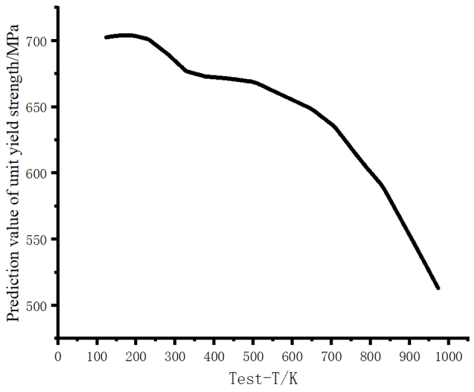


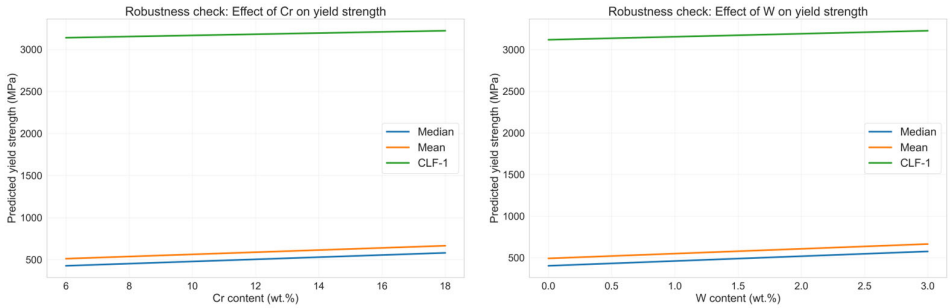
Figure 9. Effect of experimental temperature on yield strength.

From Figure 8, it can be seen that as the irradiation temperature increases, the yield strength increases, and when the temperature rises to around 800 K, the yield strength shows a decreasing trend. This is due to the irradiation hardening that occurs first with the increase in irradiation temperature in the F/M steel, resulting in an increase in yield strength; when the temperature is too high, irradiation softening occurs, and the yield strength decreases accordingly. This is consistent with the conclusion of Klueh and Harries [33] that the magnitude of irradiation hardening gradually decreases with an increasing irradiation temperature until it disappears, and a transition from irradiation hardening to softening may occur within a temperature range.

From Figure 9, it can be seen that with an increase in experimental temperature, the yield strength of irradiated F/M steel shows a significant downward trend, indicating a slowdown in the degree of irradiation hardening. Niu Ben and Wang Zhenhua [34] studied the changes in the yield strength of T91 steel at different temperatures and found that as the temperature increased, the tensile strength and yield strength of the alloy decreased but the plasticity increased, which is consistent with the model prediction results.

Next, using the trained model mentioned above, the relationship between the low-activation elements W, V, and Ta and the steel elements Mo, C, and Si and irradiation hardening was predicted. To evaluate the influence of an individual alloy element on the yield strength, other elemental content was fixed at a baseline level during the prediction, which was obtained from the median value of the mass fraction of each element in the dataset. Initially, the mass fraction of each component was C 0.089%, Cr was 9.00%, W was 1.1%, Mo was 1%, Ta was 0.59%, V was 0.20%, Si was 0.30%, Mn was 0.45%, N was 0.016%, Al was 0.015%, B was 0.403%, Cu was 0.020%, Nb was 0.030%, Ni was 0.45%, P was 0.015%, S was 0.015%, and Ti was 0.004%. The median was chosen to reduce the potential influence of outliers in the data and to obtain a more representative component center point, and all baseline values had to be within the training domain of the model

and consistent with the typical composition range of RAFM steel. The key elements Cr and W were selected, and through a robustness analysis (as shown in Figure 10a,b), it was shown that although the absolute value of the predicted yield strength varied due to the difference in components when different parameters (median, average, CLF-1 steel) were selected, the qualitative trend of the influence of each element on the yield strength always remained unchanged, which verified that the relationship between the elemental composition and the yield strength in this paper was reliable and did not change with the selection of the baseline. Taking the Cr element as an example, when establishing the relationship between the Cr element and the target variable yield strength, the other element content was fixed, and 5000 data points evenly spaced between the maximum and minimum values of the element content were generated as inputs to the prediction model. In the same way, 5000 evenly spaced data sequences were generated within the interval between the maximum and minimum values of each feature as inputs to the prediction model, and the scatter plot of the model prediction could obtain the influence of the composition on the yield strength of the irradiated steel under non-irradiation (0 dpa) and an irradiation dose of 20 dpa.



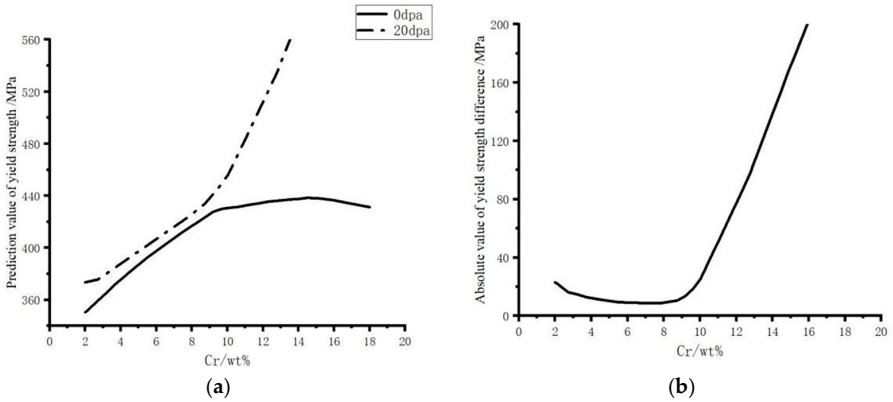
(**a**) (**b**)

Figure 10. Key element robustness graph. (**a**) Cr element robustness analysis and (**b**) Cr element robustness analysis.

Based on the current irradiation temperature inside the reactor reaching above 550 °C/823 K, the irradiation temperature in this article is selected as 550 °C/823 K. According to the actual design requirements, the irradiation dose is selected as 20 dpa. Figure 11a shows the trend of the effect of Cr element composition changes on the yield strength of F/M steel under irradiation doses of 0 dpa and 20 dpa. To clearly express the amplitude of the change in yield strength before and after irradiation, the absolute difference between the vertical axis of the two curves is taken to establish its influence trend with the composition content. The trend of the absolute difference is used to predict the effect of this composition on the degree of irradiation hardening of F/M steel. If the curve shows an upward trend, it will exacerbate the degree of radiation hardening; on the contrary, if the curve shows a downward trend, it slows down the degree of radiation hardening. Figure 11b shows the absolute prediction of the difference in the yield strength of F/M steel with the Cr element under irradiation doses of 0 dpa and 20 dpa. It can be concluded that when the Cr content is below 9.0%, the effect on irradiation hardening is not significant; when the Cr content is higher than 9.0%, it will significantly aggravate radiation hardening. Therefore, adding Cr content of 9.0% can effectively reduce the impact of radiation hardening.

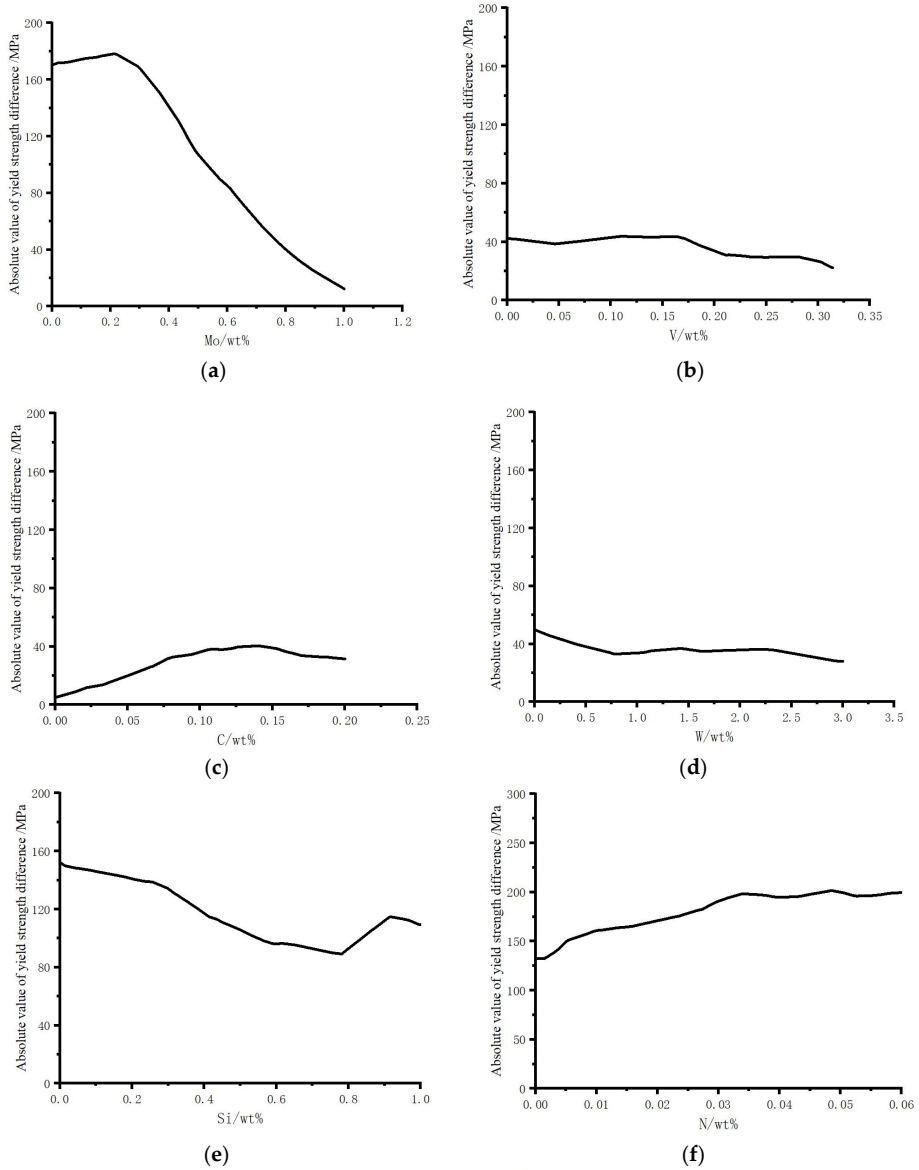
Similarly, the difference absolute value prediction diagrams of Mo, V, C, W, Si, Ta, N, Ti, and Mn component content and yield strength were established, respectively, and Mo, V, C, W, Si, and Ta were fixed as 0~200 MP, and the N, Ti, and Mn were fixed as 0~300 MPa. Figure 12a–i show the correlation relationships between the difference absolute value of

Mo, V, C, W, Ta, N, Ti, and Mn component content and yield strength under 0 dpa and 20 dpa conditions.



(**a**) (**b**)

Figure 11. Prediction of radiation hardening of F/M steel by Cr at 550 °C. (**a**) Prediction of yield strength of F/M steel with Cr content at 0 dpa and 20 dpa at 550 °C and (**b**) absolute prediction of yield strength difference with Cr content at 0 dpa and 20 dpa at 550 °C.



(**a**) (**b**) (**c**) (**d**) (**e**) (**f**)

Figure 12. *Cont.*

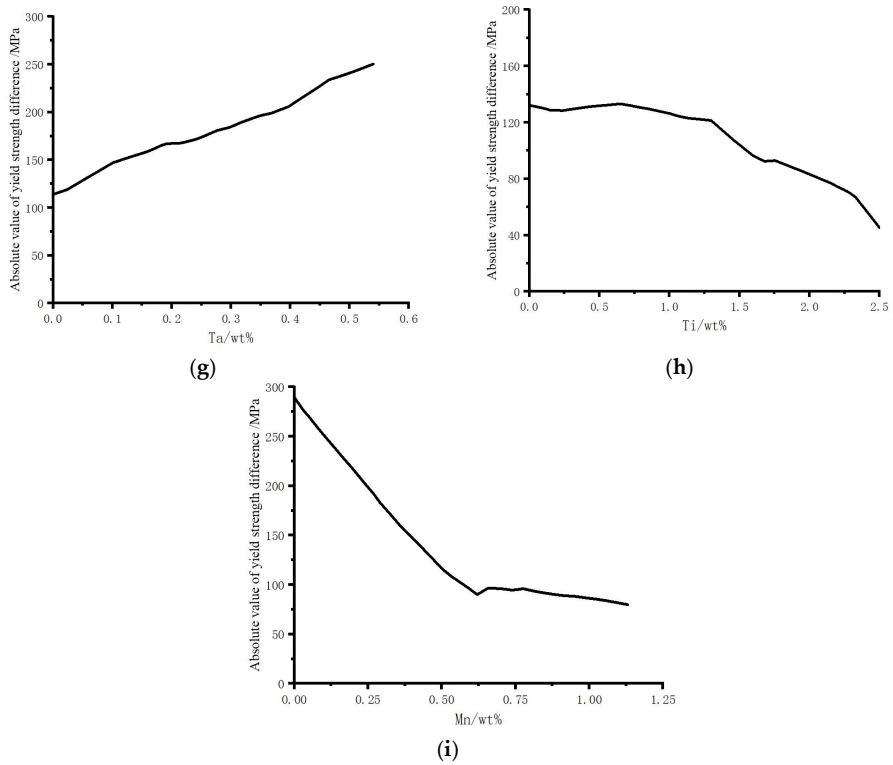


Figure 12. Absolute prediction of yield strength difference in each component at 0 dpa and 20 dpa at 550 °C. (**a**) Mo; (**b**) V; (**c**) C; (**d**) W; (**e**) Si; (**f**) N; (**g**) Ta; (**h**) Ti; and (**i**) Mn.

From Figure 12a, it can be seen that the curve first shows an upward trend in a small range, then shows a significant downward trend when the Mo content is around 0.25%, indicating that when the Mo content is higher than 0.25%, it significantly alleviates the degree of irradiation hardening of F/M steel. It can be seen from Figure 12b,d that the curve change trend is relatively flat with an increase in the content of the two elements W and V, indicating that W and V have little effect on the degree of irradiation hardening of F/M steel after irradiation. Among them, when the V content is about 0.16%, the curve has a slight downward trend, indicating that when V content is added above 0.16%, it can slightly improve the irradiation hardening effect; when the W content is less than 1.0%, the curve has a small range of decline, indicating that when W content is added below 1.0%, it can also slightly alleviate the influence of irradiation hardening. From Figure 12c, it can be seen that the curve first rises, and when the C content is higher than 0.15%, the curve gradually becomes flat, indicating that with the increase in content, the irradiation hardening effect becomes more serious, which is due to the combination of C with strong carbides. Uniform and dispersed MC-type carbides are areitated and $M_{23}C_6$-type carbides are precipitated when the C content is higher, increasing the hardness of the material [35], making the hardening effect more significant. It can be seen from Figure 12e that as the content of the Si element increases, the curve first shows a downward trend and then shows an upward trend. Among them, when the Si content reaches 0.8%, the curve rises, indicating that when the Si content is less than 0.8%, it can affect the degree of irradiation hardening of F/M steel to a certain extent; when the Si content is higher than 0.8%, the degree of irradiation hardening of F/M steel becomes more serious, and when the added Si content is about 0.8%, it is the best for improving the irradiation hardening effect of F/M steel. It can be seen from Figure 12f,g that the curve shows an overall upward trend, indicating that with the increase in the content of N and Ta elements, the degree of irradiation hardening of F/M steel is aggravated, and the curve slope of Figure 12g is larger, indicating that Ta has a more significant effect on the hardening effect. It can be seen from Figure 12h,i that the

curve shows an overall downward trend, indicating that with a change in the content of Ti and Mn elements, the irradiation hardening effect can be alleviated. Among them, when the Ti content is higher than 1.25% and Mo content is lower than 0.625%, the curve has a larger downward slope, indicating that when the Ti content is higher than 1.25% and the Mo content is lower than 0.625%, the alleviation effect on the irradiation hardening effect of F/M steel is more significant.

The model predicted the trend of the two curves of the content of Mo, V, C, Cr, and W and the yield strength of F/M steel under conditions of non-irradiation (0 dpa) and an irradiation dose of 20 dpa, analyzed the joint influence of some dual elements on the change in yield of F/M steel by combining the relevant thermal analysis chart in this paper, and focused on the comprehensive influence of dual element interaction on irradiation hardening through modeling analysis, finding the low hardening component interval of dual elements.

7. Analysis of the Effects of Biaxial Irradiation Hardening

It can be seen from the prediction results of single elements that an independent change in elements such as Cr, Mo, Si, Ta, etc., has a significant effect on the irradiation hardening effect of F/M steel. However, there is a synergistic or antagonistic effect between different elements in the actual F/steel, as revealed in the correlation analysis of Tables 3 and 4, the positive correlation of C/Cr, N/Mn, Ti/N, etc., and the negative correlation of Cr/Si, Mo/W, etc. In this section, based on the Bayesian optimization BP neural network model for single-element prediction, the interaction different element pairs is revealed, and the nonlinear influence of the interaction between double elements on the comprehensive irradiation hardening of F/M steel is quantified.

When selecting key element pairs, it is necessary to combine the bivariate component correlation coefficient and consider the contribution of SHAP values. Table 3 shows that the positive correlation coefficient between C and Cr is 0.64, and it is known that carbides are synergistically reinforced, while under radiation, carbides have defective absorption. Klimenkov et al. [36] found through atom probe tomography technology analysis that when the atomic ratio of C:Cr ≈ 1:6 in Eurofer97, the precipitation density of $M_{23}C_6$ carbide reaches the maximum, and the irradiation hardening amount also increases, which is consistent with the phenomenon that the C element will intensify the irradiation hardening phenomenon in single-element prediction, so the C-Cr element pair has selective significance. In addition, the second part of this paper investigated the segregation of the Si element at the grain boundary, which weakens the grain boundary strengthening effect of Cr, and the Cr-Si pair can be selected to verify the antagonistic effect of the two. In the SHAP analysis, Mo has the highest contribution value. Li Yalai et al. [37] confirmed through APT that Mo doping can refine the grains of W powder, and Mo is enriched at the grain boundary. Under irradiation conditions, the grain boundary is a trap to absorb vacancies, suppressing the growth of dislocation rings, thereby reducing the hardening rate; Wei et al. [38] found through atomic simulation that the W-Mo system has a higher shift threshold energy due to the difference in atomic mass, which can reduce residual defects after irradiation, so that the hardening is delayed. Therefore, the competitive inhibition mechanism of the element pair W-Mo is of research significance. Mn is a low-activation element. Liu Xiangjun et al. [39] found that the doping of Mn can increase the charge density around N, reduce the diffusion potential barrier of N, significantly improve the solid solubility stability of N, and promote the formation fine MnxNy precipitation phase, which can be used as dislocation pinning points to increase hardness. This paper selects the Mn-N element pair to verify whether N has the same synergistic strengthening effect under irradiation conditions. V is the second-lowest activation element in the SHAP analysis.

Wang Jintao et al. [40] found that adding V to Fe-Al-Cr alloy can significantly increase the high-temperature oxidation rate, while adding Si will reduce oxidation, indicating that V weakens the antioxidant capacity of Si, so this paper selects the Si-V element pair to verify its interaction type.

To sum up, this paper selects five groups of element pairs, and the selection basis and the expected types of element interaction are summarized in Table 5.

Table 5. Element pair selection.

Element Pair	Correlation Feature	Selection Criteria	Expected Interaction Type
C-Cr	Strong positive correlation (0.64)	Cooperative strengthening of carbide-forming elements	Synergistic hardening
Cr-Si	Strong negative correlation (−0.69)	Si grain boundary segregation weakens the grain boundary strengthening effect of Cr	Antagonistic inhibition
Mo-W	Moderate negative correlation (−0.53)	Fine grain of Mo, SHAP analysis shows the importance of Mo first	Competitive inhibition
N-Mn	Strong positive correlation (0.64)	Mn enhances the solubility of N, and strengthens solid solution strengthening	Synchronous reinforcement
Si-V	Weak negative correlation (−0.48)	Si enhances antioxidant, V weakens; SHAP analysis shows the importance of V second	Stochastic competition

Next, using the trained model mentioned above, other elements are fixed as the base value, the fixed value is consistent with the predicted single-element composition, and an element pair concentration matrix is generated on the two-dimensional grid. Similarly, using the trained Bayesian optimized BPNN model, the input files are sets of predicted results of single elements, with each set of single-element prediction results containing the content of element composition (wt%) and the absolute value of the difference between the absolute values of strength under 0 dpa and 20 dpa irradiation (ΔYS). Two single-element datasets are merged into a dual element combination, where discrete data are interpolated into continuous grid data, and the comprehensive irradiation hardening effect is calculated. In the generated dual-element irradiation hardening contour map, the X-axis from left to right indicates that the content of one element increases, the Y-axis from top to bottom indicates that the content of the other element increases, and the color in the figure blue → green → yellow → red indicates that the ΔYS value increases. The dark blue area indicates that ΔYS < 100 MPa, and the comprehensive radiation effect of the element pair is slight; the blue-green transition area indicates that 100 MPa ≤ ΔYS ≤ 200 MPa and the F/M steel exhibits moderate hardening at this time; the yellow area indicates that 200 MPa < ΔYS ≤ 300 M, and the irradiation hardening phenomenon of the element pair is relatively significant at this time; and the orange-red area indicates that ΔYS > 300 MPa and the F/M steel is severely hardened at this time, and may be accompanied by brittleness. The contour-dense area in the cloud map represents that the performance fluctuates violently due to the change in components, which corresponds to the sensitive area; the contour -parse area represents that the performance is affected by the change in components relatively smoothly, corresponding to the stable area. Taking the element pair of C-Cr as an example, Figure 13 represents the influence cloud map of the interaction of C-Cr on the irradiation hardening of F/M steel. When the Cr content is less than 10% and the C content is between 0 and 0.20%, there is a large blue area and the contour is sparse, indicating that the comprehensive irradiation effect of C-Cr in this interval is slight, and the change

in C and Cr content has a weak effect on irradiation hardening. Among them, when the C content is less than 0.05%, it shows a deep blue depression area, indicating that the comprehensive irradiation hardening effect of C-Cr in this interval is the weakest; when the Cr content is higher than 10% and the C content is between 0 and 1.0%, the color in the figure gradually transitions to red, and the contour gradually becomes dense, indicating that the irradiation hardening of C-Cr in this composition interval of F/M steel gradually increases, and the change in C and Cr element content has a greater effect on irradiation performance. According to the research of Liu Chenxi [41] and others, it is known that Cr in RAFM steel easily forms $Cr_{23}C_6$ precipitate phase with C, which can effectively pin the grain boundary and dislocation, enhance the thermal strength of steel in the form of precipitation strengthening, and reasonably explain the intensification of the hardening effect with an increase in Cr content.

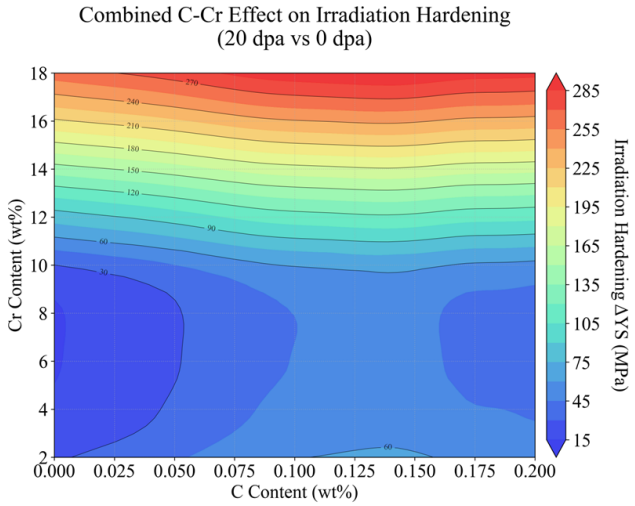


Figure 13. C-Cr irradiation hardening contour map.

To assist in identifying the synergistic and antagonistic effects in the cloud map, we quantify the nonlinear impact of binary element interactions on irradiation hardening. The code visualizes the output of the synergistic/antagonistic index cloud map and the three-dimensional visualization of the synergistic effect top, and carries out machine learning analysis. The synergistic/antagonistic index is used to quantify the nonlinear impact of a combination of two elements on irradiation hardening, and its value is defined as the deviation between the model's predicted value and the expected value of the linear hypothesis, where red regions in the synergistic/antagonistic index cloud map represent synergistic index > 30%, deep blue regions represent antagonistic index > 30%; and white regions represent neutral zones. Machine learning outputs quantify the element contribution degree and calculate the interaction strength, where SHAP values are used to measure the interaction strength between any two features (elements), and the average value of the SHAP interaction values is calculated for all samples, which can obtain the average interaction intensity of each element at the global level. To assess the relative importance of specific element interactions to the overall prediction variance, the percentage of the SHAP mean square value of this interaction term relative to the sum of the main effect mean square values of all features and all effects is calculated, and this percentage is the contribution value of this interaction to the prediction results of irradiation hardening.

Figure 14a,b show the synergistic/antagonistic index contour map and 3D synergistic effect map of the C-Cr element pair, which show that with an increase in Cr and C content, there is a strong synergistic area with deep red, indicating that the C-Cr elements affect the irradiation hardening effect of F/M steel by a synergistic mechanism. The machine learning

analysis result output shows that the content of C the element is 2.2%, the contribution of the Cr element is 97.8%, and the intensity of element interaction is 0.553, which quantifies and proves that when the C-Cr interaction occurs, they promote each other to enhance the irradiation hardening effect, and the Cr element plays a leading role in the irradiation hardening of F/M steel. This is generally consistent with the research observations of Kimura et al. on high-Cr RAFM steel, and the team's experimental results show that excessive Cr content (>10.5 wt%) will promote the irradiation-induced precipitation of rich-Cr α'phase, which is one of the main reasons for low-temperature irradiation hardening and embrittlement. Our model further quantifies this nonlinear deterioration effect and reveals that even against a high C-Cr background, a slight increase in C (such as >0.1 wt%) will sharply aggravate hardening through synergistic interaction. Radiguet et al. further confirmed through atom probe tomography (APT) that after irradiation, C tends to segregate at dis rings or Cr clusters, which may aggravate hardening by inhibiting point defect recombination or stabilizing rich-Cr clusters, which provides a potential microstructural explanation for our model. This also verifies the antagonistic effect between the C-Cr element pairs and is consistent with the single-element prediction results in Section 5, which is in line with the interaction type.

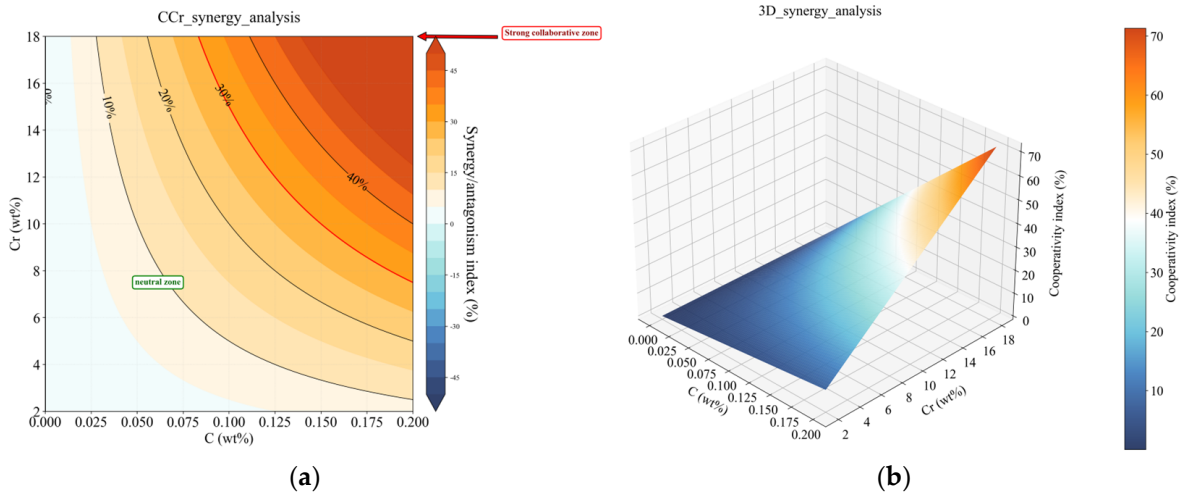


Figure 14. (**a**) C-Cr synergistic/antagonistic index cloud map and (**b**) three-dimensional synergistic effect map.

However, according to the research, there are also some differences between the prediction of this study model and the literature. For example, some studies show that C can be beneficial to radiation resistance by forming fine nano-phases such as TaC/VC, etc. The reason for this difference may be that the training data of this model is limited, the irradiation conditions are different from the literature, resulting in different damage microstructures, and the interaction is modulated by other alloy elements, while binary element analysis fixes other elements and has not considered this competitive effect for the time being.

Similarly, the influence cloud map of irradiation hardening on the elements is plotted, respectively, as shown in Figure 15a–d.

From Figure 15a, it can be seen that when the Cr content is less than 10% and the Si content is between 0 and 1.0%, there is a large area of blue region with sparse contour lines, indicating that the comprehensive irradiation effect generated by Cr-Si in interval is slight, and the change in Cr and Si element content has little effect on irradiation performance. Among them, when the Si content is between 0.6% and 0.8%, it shows a deep blue low-lying area, indicating that the comprehensive irradiation hardening effect of Cr-Si in this

interval is the lowest; when the Cr content is higher than 10% and the Si content is between 0 and 1.0%, the color in the figure gradually transitions to red and the lines gradually become dense, indicating that the irradiation hardening of Cr-Si in this composition interval gradually increases under F/M steel irradiation conditions, and the change in C-Cr element content has a greater impact on irradiation performance. The research of Tanigawa et al. partially supports this prediction. This team experimentally found that Si can inhibit the growth of vacancy clusters under irradiation conditions and reduce the coarsening of He bubbles, thus improving the radiation damage of materials to a certain extent. However, its effect strongly depends on the irradiation temperature. Our model predicts the positive role of Si in a wider composition range, and its universality needs to be further verified, especially under different doses and higher-temperature irradiation conditions. As can be seen from Figure 15b, when the Mo content is lower than 0.4% and the W content is between 0 and 3.0%, a large red area appears, indicating that the comprehensive irradiation hardening effect of Mo-W is significant in this interval, and the F/M steel experiences severe hardening. Among them, when the Mo content is between 0 and 0.3% and the W content is between 0 and 0.4%, a dark red highland area appears, indicating that the comprehensive irradiation hardening effect of Mo-W in this interval is the most serious; when the Mo content higher than 0.5% and the W content is between 0 and 3.0%, the color gradually transitions to blue, the isotherms gradually appear, and the hardening effect of the F/M steel slows down. The study of Lindau et al. on Eurofer97 and modified steel shows that the addition of W and Ta can refine the precipitation phase and improve high-temperature stability, but the specific impact on irradiation hardening is complex and lacks systematic research. However, Mo and W are both stable elements of the body-centered cubic structure, and the complex antagonistic relationship between them may be related to the competitive carbide formation and the impact of each other's solubility in the matrix, which requires more in-depth first-principles calculations or phase-field simulations to reveal its atomic-scale mechanism. As can be seen from Figure 15c, when the Mn content is higher than 0.5% and the N content is between 0 and 0.06%, there is a large area of blue region and the contour lines are sparse. Within this interval, the comprehensive irradiation hardening of Mn-N is slight. Among them, when the Mn content is between 0.6% and 1.1% and the N content is between 0 and 0.01%, there is a dark blue region, and the comprehensive irradiation hardening effect of Mn-N in this interval is the smallest. When the Mn content is lower 0.5% and the N content is between 0 and 0.06%, with a decrease in Mn content and an increase in N content, this gradually transitions to the red region, the contour lines gradually become dense, and the irradiation hardening effect of Mn-N intensifies. The content change in Mn and N has a large impact on irradiation performance. It can be seen from Figure 15d that when the Si content is lower than 0.8% and the V content is between 0 and 0.3%, the area gradually transitions from red to blue and the comprehensive irradiation hardening effect of Si-V gradually slows down. Among them, when the Si content is between 0 and 0.1% and the V content is between 0 and 0.17%, there is a dark red region, and the comprehensive irradiation hardening effect of Si-V in this interval is the most serious. When the Si content is between 0.3% and 0.8% and the V content is between 0.2% and 0.3%, there is a dark blue region, and the comprehensive irradiation hardening effect of Si-V this interval is the weakest. When the Si content is higher than 0.8%, as the Si and V content increases, the area gradually changes from blue to yellow and the irradiation hardening effect of F/M steel intensifies.

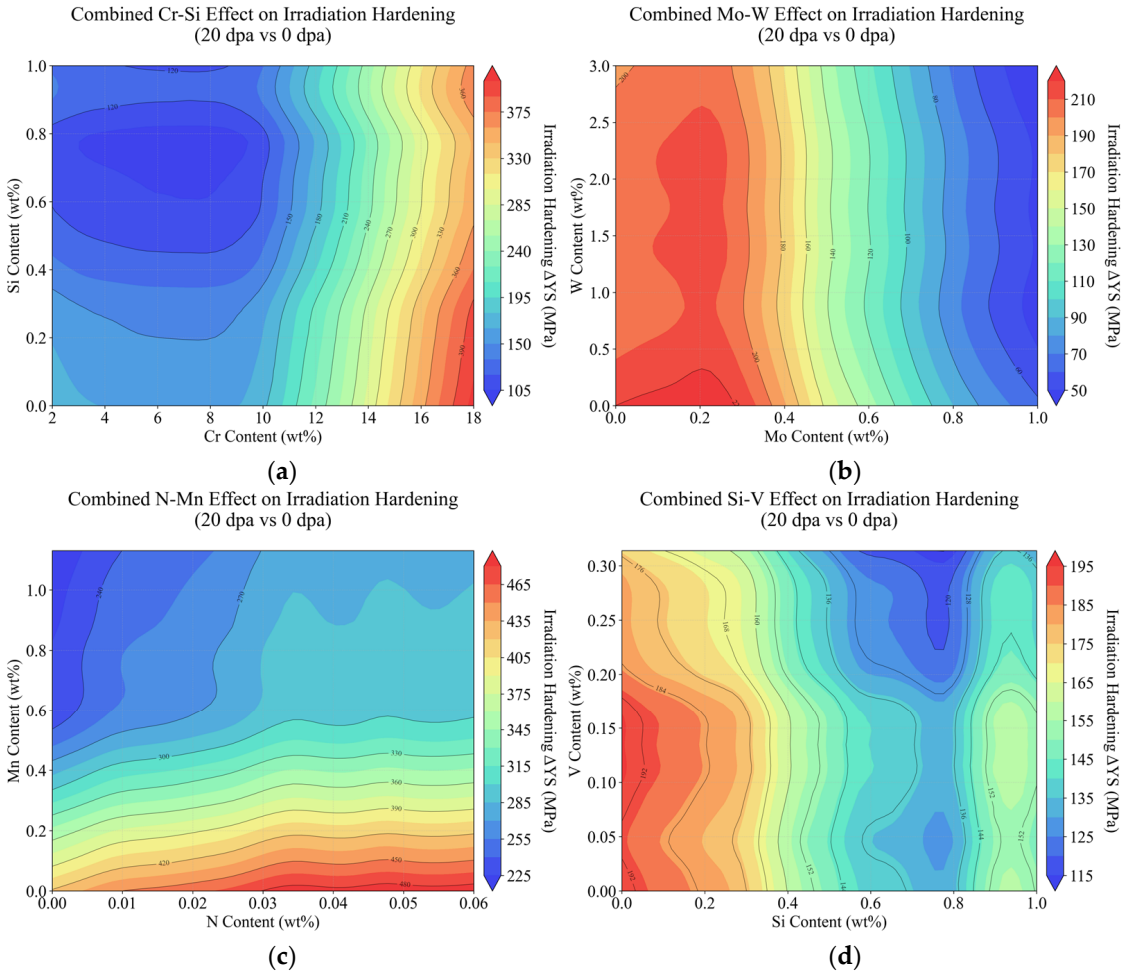


Figure 15. (**a**) Cr-Si irradiation hardening contour map; (**b**) Mo-W irradiation hardening contour map; (**c**) N-Mn irradiation hardening contour map; and (**d**) Si-V irradiation hardening contour map.

Figure 16a–d show the synergistic/antagonistic index contour map and 3D visualization of the synergistic effect topography of the element pairs Cr-Si, Mo-W, N-Mn, and Si-V, respectively. In Figure 16a,b, the deep blue area gradually appears with an increase in the abscissa and ordinate, and the map in Figure 16a appears earlier, indicating that Cr-Si and Mo-W affect the irradiation hardening effect of F/M steel by an antagonistic mechanism, and the antagonism among Cr-Si is stronger. In Figure 16c, the synergistic/antagonistic index contour map is shown as a neutral zone, but it can be seen from the 3D visualization of the synergistic topography that with an increase in the content of N and Mn elements, a smaller part of the orange red surface appears, indicating that there is a weak synergistic effect of N-Mn elements. In Figure 16d, the synergistic/antagonistic index contour map also shows a neutral zone, and it can be seen from the 3D visualization of the synergistic effect topography that with an increase in the content of Si and V elements, a smaller part of the blue surface appears, indicating that there is a weak antagonistic effect between Si-V elements.

In addition, the machine learning analysis results of Cr-Si, Mo-W, N-Mn, Si-V, and Cr-Si are shown in Table 6, where an interaction strength of >0 is synergistic and <0 is antagonistic; the sum of the element contribution values = 100%.

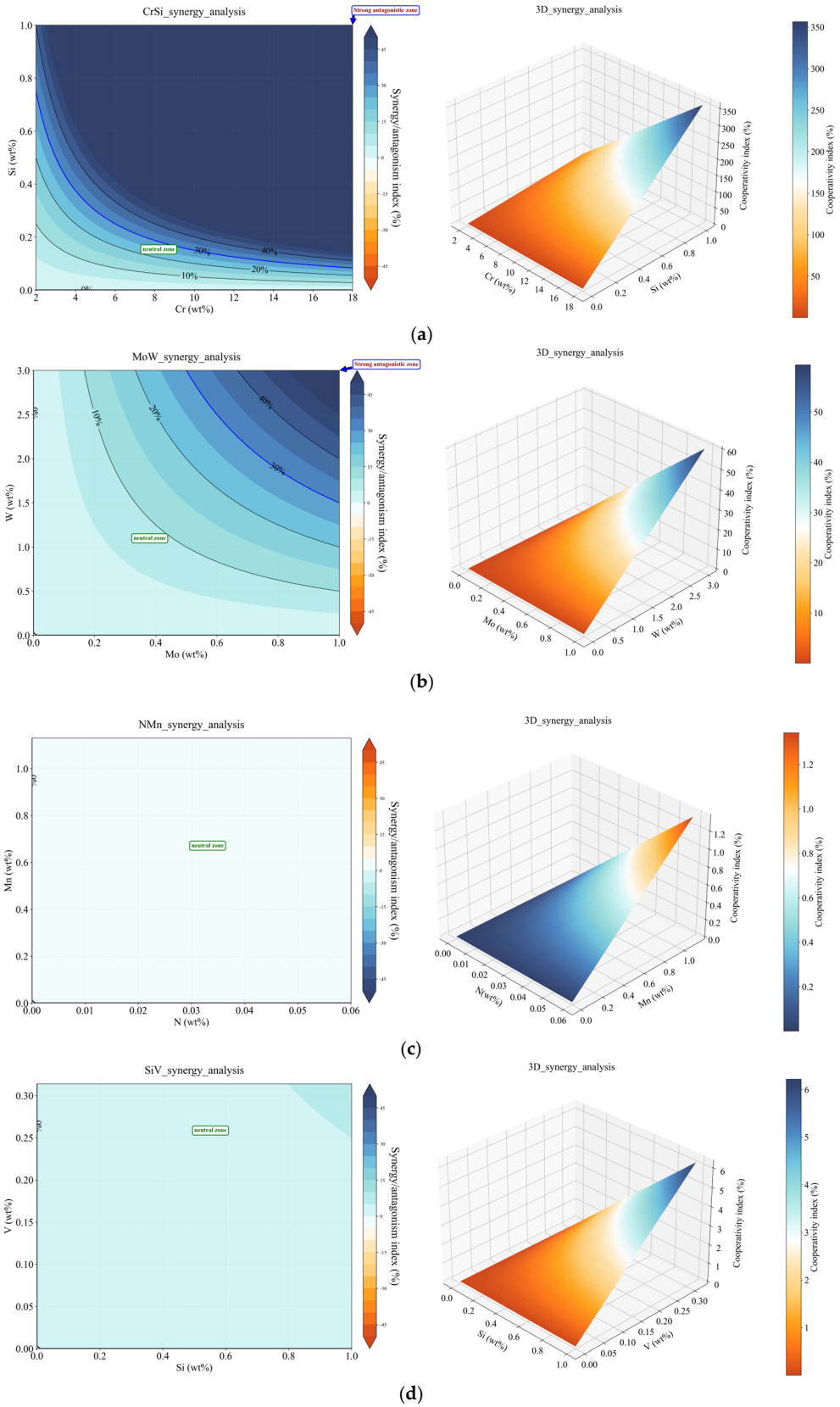


Figure 16. (**a**) C-Cr synergistic/antagonistic index cloud map and synergistic effect topography three-dimensional visualization; (**b**) Mo-W synergistic/antagonistic index cloud map and synergistic effect topography three-dimensional visualization; (**c**) N-Mn synergistic/antagonistic index cloud map and synergistic effect topography three-dimensional visualization; and (**d**) Si-V synergistic/antagonistic index cloud map and synergistic effect topography three-dimensional visualization.

Table 6. Machine learning analysis results.

Element Pair	Element 1 Contribution Value	Element 2 Contribution Value	Interaction Strength	Analysis Results
Cr-Si	77.2%	22.8%	−0.833	Mutual inhibition, weakening the radiation hardening effect, and the Cr element plays a leading role
Mo-W	98.3%	1.7%	−0.562	Mutual inhibition, weakening the radiation hardening effect, and Mo element plays a leading role
N-Mn	9.7%	90.3%	0.377	Promote each other, enhance the radiation hardening effect, and the Mn element plays a leading role.
Si-V	89.0%	11.0%	−0.311	Mutual inhibition, weakening the radiation hardening effect, and the Si element plays a leading role.

This research systematically predicted the interaction of key element pairs and their influence on radiation hardening in F/M steels using machine learning, revealing complex nonlinear effects beyond conventional single-element analysis frameworks. The model predictions in terms of C-Cr synergy and Cr-Si antagonism show a certain agreement with the results exhibited in some of the experimental literature, enhancing confidence in the model's interpolation in the compositional space and indicating that machine learning models can capture and quantify certain physical mechanisms observed in experiments. There are also discrepancies and uncertainties. The model predictions for Mo-W, N-Mn, and Si-V, etc., show more novelty or differences from others. These discrepancies and uncertainties stem from the following three main aspects. First, data-driven limitations: the model's performance highly relies on the quantity, quality, and coverage of the training data. Noise in the data, systematic errors (e.g., differences between ion and neutron irradiation), and the complex coupling relationship between composition–process–radiation conditions all introduce prediction uncertainties. Second, challenges in mechanism interpretation: machine learning models are good at finding correlations but still require physical insights to explain causality. The predicted element interactions should be combined with thermodynamic calculations, microstructure characterization should be performed, and multiscale simulations should be translated into reliable physical mechanism understanding. Third, extrapolation risk: there is a risk in for composition regions that are not well covered by the training data (e.g., ultra-high Cr, high C regions). Predictions in these regions should be regarded as "hypothesis generation" and prioritized for experimental validation.

Through the analysis of bivalent interaction, the synergistic hardening mechanism of C-Cr and N-Mn and the antagonistic mechanism of Cr-Si, Mo-V, and Si-V, which comprehensively influence the irradiation hardening effect of F/M, were revealed, the sensitive area and optimization area of b components were predicted, and the nonlinear influence of bivalent interaction was quantified, which broke through the limitations of traditional single-element design and provided a new dimension for the multi-objective composition of F/M steel. Subsequently, the influence of ternary combination on irradiation hardening will be analyzed in combination with the calculation of a ternary phase diagram. It can be concluded that the composition design scheme within a certain range can be achieved under specific temperature conditions.

8. Conclusions

This paper collects 2048 sets of radiation hardening data of F/M steel, including composition, process, and performance, etc., and 2014 sets of data suitable for machine learning through preliminary data cleaning, feature screening, and source and correlation analysis. The Bayesian optimization BP neural network is used to construct a regression model of the alloy composition of F/M steel and its yield strength at the irradiation temperature of 550 °C/823 K, and the determination coefficient R^2 reaches 0.8124. Through the trend of the prediction curve of the difference absolute value of the yield strength of each characteristic component at irradiation doses of 0 dpa and 20 dpa, the correlation between the key components and the radiation hardening of F/M steel is obtained, and the sensitivity area and the optimization area of the double element combined component are found through the interaction analysis of the double elements. The following conclusions are drawn:

(1) Combined with the double-element correlation analysis, it is found that P, S, Si, and B elements mutually enhance the influence on the yield of F/M steel, and C and Cr elements also mutually enhance the yield strength of F/M steel; Cr and P, S, Si, W, C, P, and B, respectively, mutually weaken the influence on the yield strength of F/M steel, and Mo, W, and Ta also mutually weaken the yield strength of F/M steel.

(2) Combined with unary element prediction analysis, it is concluded that the content of Cr has a greater impact on the irradiation hardening of F/M steel, and when the content of Cr is about 9.0% higher, it will greatly aggravate the irradiation hardening. It is more beneficial to the irradiation resistance of F/M steel when the content of Cr is selected to be about 9.0%; when the content of Mo is added to be about 0.2% higher, the content of Si is added to be about 0.8% higher, and when Ti and Mn are added, the irradiation hardening degree of F/M after irradiation can be significantly alleviated.

(3) The addition of W and V has a lesser effect on the degree of irradiation hardening of F/M steel after irradiation, and when the content of addition is higher than about 0.16% and the content of W addition is lower than about 1.0%, it can improve the irradiation hardening effect a lesser extent, while the addition of N, Ta, and C will aggravate its irradiation hardening.

(4) Combined with the analysis of double-element interaction, it is concluded that when the content of C in C-Cr is higher than 0.05% and the content of Cr is higher than 10%, there is a strong synergistic area, which will cause serious hardening and must be strictly avoided; N-n shows a weak synergistic effect, and N needs to be controlled to be lower than 0.01% to avoid the hardening of F/M steel.

(5) When the content of Cr in Cr-Si is less than 10% and the content of Si is between 0.6% and 0.8%, it is a strong antagonistic area, and the lowest comprehensive irradiation hardening effect can be achieved in the 9Cr-0.8Si combination; in MoW, when the Mo is low and the W is high, a hardening peak appears, which needs to be avoided, and the Mo content needs to be controlled to be higher 0.5% to alleviate irradiation hardening; Si-V shows a weak antagonistic area, and when the content of Si is between 0.3% and 0.8% and the content of V is between 0.2% and 0.3%, it can assist in optimizing the composition of F/M steel.

(6) The quantitative contribution of elements indicate that Cr (77.2%), Mo (98.3%), Mn (90.3%), and Si (89.0%) dominate the interaction.

The relationship between irradiation hardening and Mo, Cr, C, W, and other elements, as well as the interaction between dual elements such as C-Cr and Cr-Si, was predicted. In addition, the influence of the three-element combination on the change in yield strength was analyzed by combining the three-element phase diagram. In the later stage, the multi-element synergistic mechanism among P, S, Si, and B elements and the multi-element

antagonistic mechanism between Cr, C, and Si elements could be focused on. A composition design scheme of F/M steel with a lower irradiation hardening degree under certain irradiation conditions was obtained.

Author Contributions: Y.H.: conceptualization, methodology, software, investigation, formal analysis, writing—original draft. B.B.: conceptualization, funding acquisition, resources, supervision, writing—review and editing. J.B.: investigation, data curation. S.W.: data curation, validation. X.H.: resources, supervision. W.Y.: resources, supervision. All authors have read and agreed to the published version of the manuscript.

Funding: This project is funded by the Stable Support Research Project of the Ministry of Finance of China (BJ020261223286) and Youth Talent Project of China National Nuclear Corporation (FY222506000902) and The President Funding of CIAE (YZ232602000702).

Data Availability Statement: The data presented in this study are not publicly available due to privacy and ethical restrictions. The data contain sensitive personal information that could compromise research participant privacy and consent.

Conflicts of Interest: The authors declare that they have no known competing financial interests or personal relationships that could have appeared to influence the work reported in this paper.

References

1. Xu, Y.; Lv, Y.; Zhou, H.; Luo, G. Research progress and prospects of fusion reactor blanket structure materials. *Mater. Sci. Technol.* **2018**, *32*, 2897–2906.
2. Yu, X.; Song, Y.; Cui, S.; Li, M.; Li, Z. Research Status and Progress of Structural Materials for Reactors. *Mater. Sci. Technol.* **2008**, *2*, 68–72.
3. Huang, Q.; Li, J.; Wu, Y.; Yu, J.; Wan, F. Development of low activation martensitic steel for fusion reactors. *Nuclear Sci. Eng.* **2004**, *24*, 56–64.
4. Li, X.G.; Yan, Q.Z.; Ge, C.C. Research progress of reduced activation ferritic/martensitic steels. *J. Iron Steel Res.* **2009**, *21*, 6. (In Chinese)
5. Chaouadi, R. Effect of irradiation-induced plastic flow localization on ductile crack resistance behavior of a 9% Cr tempered martensitic steel. *J. Nucl. Mater.* **2008**, *372*, 379. [CrossRef]
6. Fave, L.; Pouchon, M.A.; Döbeli, M.; Schulte-Borchers, M.; Kimura, A. Helium ion irradiation induced swelling and hardening in commercial and experimental ODS steels. *J. Nucl. Mater.* **2014**, *445*, 235–240. [CrossRef]
7. Mosbrucker, P.L.; Brown, D.W.; Anderoglu, O.; Balogh, L.; Maloy, S.; Sisneros, T.; Almer, J.; Tulk, E.; Morgenroth, W.; Dippel, A. Neutron and X-ray diffraction analysis of the effect of irradiation dose and temperature on microstructure of irradiated HT-9 steel. *J. Nucl. Mater.* **2013**, *443*, 522–530. [CrossRef]
8. Gaganidze, E.; Petersen, C.; Materna-Morris, E.; Dethloff, C.; Weiß, O.; Aktaa, J.; Povstyanko, A.; Fedoseev, A.; Makarov, O.; Prokhorov, V. Mechanical properties and TEM examination of RAFM steels irradiated up to 70dpa in BOR-60. *J. Nucl. Mater.* **2011**, *417*, 93–98. [CrossRef]
9. Tanigawa, H.; Sakasegawa, H.; Hashimoto, N.; Klueh, R.; Ando, M.; Sokolov, M. Irradiation effects on precipitation and its impact on the mechanical properties of reduced-activation ferritic/martensitic steels. *J. Nucl. Mater.* **2007**, *367–370*, 42–47. [CrossRef]
10. Huang, Q.; Li, C.; Li, Y.; Chen, M.; Zhang, M.; Peng, L.; Zhu, Z.; Song, Y.; Gao, S. Progress in development of China Low Activation Martensitic steel for fusion application. *Nucl. Mater. Energy* **2018**, *16*, 191–197. [CrossRef]
11. Huang, Q.; Wang, X.; Sun, S.; Liu, Y.; Liao, H.; Zheng, P.; Peng, L.; Zhai, Y. Development of reduced activation ferritic/martensitic steels in China. *J. Nucl. Mater.* **2022**, *568*, 153887. [CrossRef]
12. Castin, N.; Malerba, L.; Chaouadi, R. Prediction of radiation induced hardening of reac tor pressure vessel steels using artificial neural networks. *J. Nucl. Mater.* **2011**, *408*, 30–39. [CrossRef]
13. Cottrell, G.A.; Kempk, R.; Bhadeshi, H.; Odette, G.; Yamamoto, T. Neural network analysis of Charpy transition temperature of irradiated low-activation martensitic steels. *J. Nucl. Mater.* **2007**, *367–370*, 603–609. [CrossRef]
14. Bai, B.; Han, X.; Cao, H.; Ke, Y.; He, X.; Yang, W. Radiation hardening prediction for ODS alloy based on deep neural net work. *At. Energy Sci. Technol.* **2021**, *55*, 1184–1190.
15. Wang, P.; El-Fallah, G.M.A.M. A Data-driven machine learning model for radiation-induced DBTT shifts in RAFM steels. *J. Nucl. Mater.* **2025**, *615*, 155984. [CrossRef]
16. Wang, P.; Tao, Q.; Dong, H.; El-Fallah, G.M.A.M. Advanced machine learning analysis of radiation hardening in reduced-activation ferritic/martensitic steels. *Comput. Mater. Sci.* **2025**, *251*, 113773. [CrossRef]

17. Gibbons, J.D.; Chakraborti, S. *Nonparametric Statistical Inference: Revised and Expanded*; CRC Press: Boca Raton, FL, USA, 2014.
18. Bao, J.; Bai, B.; Ke, Y.; Gao, J.; He, X.; Yang, W. Analysis of the Influence of High Temperature Strength on Mo Based Alloys Based on Bayesian Optimization. *At. Energy Sci. Technol.* **2024**, *58*, 121–130.
19. Kang, R.; Liu, G.; Hu, B.; Hu, J.; Wu, K.; Xu, K. Optimization Design of LowActivation F/M Steel for Fuel Cladding Tube in Supercritical Water-Cooled Reactor. *At. Energy Sci. Technol.* **2009**, *43*, 523–528.
20. Shang, Y.; Fan, M.; Jiang, S.; Zhang, Z. Effects of carbon content on the microstructure and tensile properties of a low-density steel. *Int. J. Miner. Metall. Mater.* **2025**, *32*, 391–401. [CrossRef]
21. Jitsukawa, S.; Tamura, M.; van der Schaaf, B.; Klueh, R.L.; Alamo, A.; Petersen, C.; Schirra, M.; Spaetig, P.; Odette, G.; Tavassoli, A.; et al. Development of an extensive database of mechanical and physical properties for reduced-activation martensitic steel F82H. *J. Nucl. Mater.* **2002**, *307–311*, 179–186. [CrossRef]
22. An Yan, J.; Suzuki, S.; Kimura, H. Chemical bonding state of phosphorus segregated in the grain boundary of Iron and Steel. *J. Iron Steel Inst. Jpn.* **1983**, *69*, 625.
23. Yin, L.; Sridhar, S. Effects of Residual Elements Arsenic, Antimony, and Tin on Surface Hot Shortness. *Metall. Mater. Trans. B* **2011**, *42*, 1031–1043. [CrossRef]
24. Jones, R.H.; Baer, D.R.; Charlot, L.A.; Thomas, M.T. Grain boundary segregation of sulfur and antimony in iron alloys. *Metall. Trans. A* **1988**, *19*, 2005–2011. [CrossRef]
25. Huang, M. Study on the Relationship and Mechanism of Solute Elements on the Grain Boundary Bonding of Austenitic Steel. Ph.D. Thesis, North China University of Science and Technology, Tangshan, China, 2023.
26. Ebner, A.S.; Jakob, S.; Clemens, H.; Pippan, R.; Maier-Kiener, V.; He, S.; Ecker, W.; Scheiber, D.; Razumovskiy, V.I. Grain boundary segregation in Ni-base alloys: A combined atom probe tomography and first principles study. *Acta Mater.* **2021**, *221*, 117354. [CrossRef]
27. Li, F. Prediction of compressive strength of concrete based on artificial neural network model. *Compr. Util. Fly Ash* **2023**, *37*, 126–133.
28. Wu, M.; Zhang, D. A review of BP neural network improvement and its application in non-destructive testing. *China Test.* **2023**, *49*, 1–6.
29. Lundberg, S.M.; Lee, S.I. A unified approach to interpreting model predictions. In Proceedings of the 31st International Conference on Neural Information Processing Systems, Long Beach, CA, USA, 4–9 December 2017.
30. Huang, X. Research on Hardening and Embrittlement of CLAM Steel in Near ITER Dose Neutron Irradiation and Effects. Ph.D. Thesis, University of Science and Technology of China, Hefei, China, 2018.
31. Feng, X.; Yan, F.; Shen, D.; Han, G. Research on Minimum Wall Thickness Prediction of Pressure Vessels Based on Bayesian Optimization BP Neural Network. *Sci. Technol. Innov.* **2024**, *5*, 69–72.
32. Odette, G.R.; Alinger, M.J.; Wirth, B.D. Recent developments in irradiation-resistant steels. *Annu. Rev. Mater. Res.* **2008**, *38*, 471–503. [CrossRef]
33. Kohyama, A.; Hishinuma, A.; Gelles, D.S.; Klueh, R.L.; Dietz, W.; Ehrlich, K. Low-activation ferritic and martensitic steels for fusion application. *J. Nucl. Mater.* **1996**, *233*, 138–147. [CrossRef]
34. Niu, B.; Wang, Z.; Pan, Q.; Liu, C.; Wang, C.; Dong, C. Research progress on properties and composition of ferritic/martensitic heat-resistant steel for nuclear power. *Mater. Rev.* **2020**, *34*, 19141–19151.
35. Taneike, M.; Sawada, K.; Abe, F. Effect of carbon concentration on precipitation behavior of M23C6 carbides and MX carbonitrides in martensitic 9Cr steel during heat treatment. *Metall. Mater. Trans. A* **2004**, *35*, 1255–1262. [CrossRef]
36. Klimenkov, M.; Jäntsch, U.; Lindau, R. Effect of irradiation temperature on microstructure of ferritic-martensitic ODS steel. *J. Nucl. Mater.* **2019**, *522*, 240–249.
37. Li, Y.; Tan, D.; Yang, X. Influence of Mo doping in APT on the preparation of W. *Powder Metall. Ind.* **2014**, *24*, 8–11.
38. Wei, G.; Byggmästar, J.; Cui, J.; Nordlund, K.; Ren, J.; Djurabekova, F. Effects of lattice and mass mismatch on primary radiation damage in W-Ta and W-Mo binary alloys. *J. Nucl. Mater.* **2023**, *583*, 154534. [CrossRef]
39. Liu, X.; Yang, J.; Jia, G. First-principles study of the site occupation and structure of V, Mn, Mg in α-Fe(N). *J. Rare Earths* **2019**, *43*, 1357–1362.
40. Vogel, F.; Ngai, S.; Zhou, X.Y.; Zaiser, E.; Manzoni, A.M.; Wu, Y.; Zheng, W.W.; Zhang, P.; Thompson, G.B. Tracking maze-like hierarchical phase separation behavior in a Fe-Si-V alloy. *J. Alloys Compd.* **2023**, *968*, 172157. [CrossRef]
41. Liu, C.; Mao, C.; Cui, L.; Zhou, X.; Yu, L.; Liu, Y. Research progress on microstructure control and solid phase bonding of low activation ferritic/martensitic steel. *Acta Metall. Sin.* **2021**, *57*, 1521–1538.

Disclaimer/Publisher's Note: The statements, opinions and data contained in all publications are solely those of the individual author(s) and contributor(s) and not of MDPI and/or the editor(s). MDPI and/or the editor(s) disclaim responsibility for any injury to people or property resulting from any ideas, methods, instructions or products referred to in the content.